ods for calculating the average residual value.) In MAF, the size of the acceleration parameter sequence is adjusted to give best convergence. In the Newton-Orthomin algorithm, the number of orthogonal vectors used within Orthomin (k) and the Orthomin accuracy level are also tuned for optimal convergence (more details can be found in Ref. 8). All of the results for the measured CPU times are summarized in Table 1.

The first test is a parabolic airfoil with an 80×30 mesh. From Table 1 we can see that the Newton-Orthomin algorithm is 3.3 times as fast for subsonic flow ($M_\infty = 0.7141$) and is 4.2 times as fast for transonic flow ($M_\infty = 0.8016$). In the transonic cases we have higher speedups as the convergence of MAF slows down considerably, whereas the Newton-Orthomin algorithm slows down much less. The solution for the transonic case (identical for both algorithms) and the convergence of the two algorithms is shown in Fig. 1.

The second test is a NACA 64A006 airfoil for the same conditions. Table 1 shows the results of CPU time comparisons between the Newton-Orthomin algorithm and MAF in subsonic ($M_\infty = 0.8004$) and transonic ($M_\infty = 0.8663$) conditions. The results are nearly the same as those found for the parabolic airfoil. The Newton-Orthomin algorithm is 2.7 times as fast as MAF in subsonic flows and 3.8 times as fast in transonic flows. The convergence history (not shown) is very similar to the one shown in Fig. 1 for the parabolic airfoil.

The effect of increasing the size of the system is investigated by using a finer 160×60 mesh. This quadruples the number of equations in the system. The average residual value should be adjusted according to the mesh size (the double mesh has four times larger residual). The average residual for exit was 10^{-3} for the 80×30 mesh and 4×10^{-3} for the 160×60 mesh. The results of the test using a 12% thick parabolic airfoil for transonic flow ($M_\infty = 0.8016$) are given in Table 1. We see that, as the size of the system is increased, the ratio of CPU times required for the larger mesh is much less for the Newton-Orthomin algorithm. Speedups increase from 2.1 for the regular mesh to 3.9 for the fine mesh. Similar results were found for different Mach numbers and average residuals. We expect the speedup to increase further for very large systems, as the ones used in three-dimensional calculations.

Concluding Remarks

A new efficient algorithm is introduced for the solution of the two-dimensional TSD equation. The new algorithm uses Newton's method to solve the nonlinear system of equations resulting from the discretization using finite differences. An efficient iterative linear solver (i.e., Orthomin) is used for the solution of the sparse linear system of equations in each Newton step. The proposed algorithm is compared with a traditionally used approximate factorization algorithm with monotone switches (MAF). The results show 2.1 to 4.5 speedups for various cases and mesh sizes. These speedups are expected to be higher in very large systems. The results justify the viability of our algorithm. The algorithm idea can be extended for different switches, more complex flow models (i.e., Euler and Navier-Stokes equations), and configurations (i.e., three-dimensional flow). Other iterative linear solvers and different preconditioners should be tried to increase efficiency and demonstrate the robustness of this new approach.

Acknowledgments

This work was supported by the Minnesota Supercomputer Institute and the Army High Performance Computing Research Center (AHPCRC) at the University of Minnesota.

References

[1]Ballhaus, W. F., Jameson, A., and Albert, J., "Implicit Approximate Factorization Schemes for Steady Transonic Flow Problems," *AIAA Journal,* Vol. 16, No. 6, 1978, pp. 573–579.

[2]Goorjian, P. M., Meagher, M. E., and Van Buskirk, R. D., "Monotone Switches in Implicit Algorithms for Potential Equations Applied to Transonic Flows," *AIAA Journal,* Vol. 23, No. 4, 1985, pp. 492–498.

[3]Vinsome, P. K. W., "Orthomin, An Iterative Method for Solving Sparse Sets of Simultaneous Linear Equations," Society of Petroleum Engineers of AIME, Paper SPE 5729, Feb. 1976.

[4]Ma, S., and Chronopoulos, A. T., "Implementation of Iterative Methods for Large Sparse Nonsymmetric Linear Systems on a Parallel Vector Machine," *International Journal of Supercomputing Applications,* Vol. 4, No. 4, Winter 1990, pp. 9–24.

[5]Meijerink, J. A., and van der Vorst, H. A., "An Iterative Solution Method for Linear Systems of Which the Coefficient Matrix is a Symmetric M-Matrix," *Mathematics of Computation,* Vol. 31, No. 137, 1977, pp. 148–162.

[6]Hafez, M., and Palaniswamy, S., "Calculations of Transonic Flows with Shocks Using Newton's Method and a Direct Solver, Part I: Potential Flows." *Advances in Computer Methods for Partial Differential Equations,* VI, edited by R. Vichnevesky and R. Stepleman, IMACS, 1987, pp. 507–516.

[7]Lyrintzis, A. S., Wissink, A., and Chronopoulos, A. T., "The Use of Efficient Iterative Methods for Solving the Transonic Small Disturbance Equation," Univ. of Minnesota Supercomputer Inst. Research Rept. UMSI 91/288, Minneapolis, MN, Nov. 1991.

[8]Wissink, A. M., "Efficient Transonic Flow Calculations," Minnesota Supercomputer Inst., Final Project Rept., Minneapolis, MN, Aug. 1991.

Approximate Riemann Solver for Hypervelocity Flows

P. A. Jacobs*
NASA Langley Research Center, Hampton, Virginia 23665

Nomenclature

a	= local speed of sound, m/s
E	= total energy, J/kg
e	= specific internal energy, J/kg
h	= specific enthalpy, J/kg
M	= Mach number
P	= pressure, Pa
Pr	= Prandtl number, $(C_p\mu/k)$
R	= gas constant, J/kg/K
T	= temperature, K
t	= time, s
$\bar{U}$	= Riemann invariant
u	= x component of velocity, m/s
v	= y component of velocity, m/s
ws	= wave speed, m/s
x	= x (axial) coordinate, m
y	= y (radial) coordinate, m
Z	= intermediate variable
ρ	= density, kg/m^3
γ	= ratio of specific heats
μ	= coefficient of viscosity, Pa.s

Subscripts

e	= boundary-layer edge condition
L, R	= left state, right state, respectively
MIN	= minimum allowable value
x, y	= Cartesian components

Superscript

*	= intermediate states for the Riemann solver locally tangent to the cone surface

Received Sept. 23, 1991; revision received March 30, 1992; accepted for publication March 31, 1992.

*Visiting Scientist, Institute for Computer Applications in Science and Engineering; currently Research Fellow, Department of Mechanical Engineering, University of Queensland, St Lucia 4072, Australia.

I. Introduction

In recent years the proliferation of relatively fast computers has popularized the direct calculation of viscous, compressible flows in a time-accurate manner. In some situations, such as the transient hypersonic flow over a model in a shock tunnel, numerical simulation is the only way to extract detailed information about the flowfield. Such computations are very demanding since there are both strong shocks and rarefactions and strong viscous interactions. At each time step of a finite volume simulation of the flow, we first interpolate the flow state (consisting of a set of values for ρ, u, v, e, P, and a) to either side of each interface at the start of the time step and then apply a Riemann solver to estimate the flow state at the interface during the time step.

There are a number of Riemann solvers that can be used, including "exact" iterative schemes[1] and approximate (noniterative) schemes.[2,3] The approximate schemes are generally less computationally expensive than the iterative schemes, and because the Riemann solver consumes a large fraction of the total computational effort, an approximate scheme is favored. Although the Roe-type solver is popular because it is relatively fast, there are situations such as the double-Mach-reflection case[4] and flow over a sphere[5] where it may produce spurious results. The Osher-type solver[3] is considered to be fairly robust and free of adjustable parameters; however, we have experienced some difficulty in applying it to flows with very strong shocks. Here, we take a middle road between the fully iterative solvers and the single-step approximate solvers and, at the cost of some computational expense, produce an approximate solver that is reliable in extreme flow situations and is vectorizable with current compilers for vector computers.

II. Approximate Riemann Solver

The current solver is a three-stage approximate Riemann solver in which the first stage computes the intermediate pressure and velocity assuming isentropic wave interaction. A second stage, based on the strong shock relations, may be invoked to improve the first-stage estimate if the pressure jump across either wave is sufficiently large. In practice, this modification has been required only in extreme conditions such as those found in the bluff-body test case (Sec. III.A). The final stage is to select/interpolate the interface state (ρ, u, v, e, P, etc.) from the set of left, right, and intermediate states. If stage 2 (strong shock modification) is not invoked, the solver is much like Osher's approximate Riemann solver.[3]

A. Stage 1

The first stage of the Riemann solver assumes that a spatially constant left state (subscript L) and right state (subscript R) interact through a pair of finite-amplitude (and isentropic) compression or rarefaction waves. Perfect gas relations (Ref. 6 cited in Ref. 1) are used to obtain the intermediate states (L^*, R^*) in the gas after the passage of left-moving and right-moving waves, respectively. The expressions implemented in the code are

$$P_L^* = P_R^* = P^* = P_L\left[\frac{(\gamma-1)(\bar{U}_L-\bar{U}_R)}{2a_L(1+Z)}\right]^{2\gamma/(\gamma-1)} \tag{1}$$

$$u_L^* = u_R^* = u^* = \frac{\bar{U}_L Z + \bar{U}_R}{1+Z} \tag{2}$$

where the Riemann invariants are

$$\bar{U}_L = u_L + \frac{2a_L}{\gamma-1}$$

$$\bar{U}_R = u_R - \frac{2a_R}{\gamma-1} \tag{3}$$

and the intermediate variable Z is given by

$$Z = \frac{a_R}{a_L}\left(\frac{P_L}{P_R}\right)^{(\gamma-1)/(2\gamma)} \tag{4}$$

Note that these expressions involve the power operator that is computationally expensive. For a limited range of base and exponent, the standard power function is replaced by the approximate expansion.[7] In the exceptional situation of $(\bar{U}_L - \bar{U}_R) < 0$, we assume that a (near) vacuum has formed at the cell interface and set all of the interface quantities to minimum values.

B. Stage 2

If the pressure jump across either wave is large (say, a factor of 10), then the guess for the intermediate pressure is modified using the strong shock relations. Taking the large Mach number limit of the normal shock relations, the strong shock relations for a left-moving shock are

$$\frac{P^*}{P_L} \simeq \frac{2\gamma M_L^2}{(\gamma+1)}, \quad \frac{\rho_L^*}{\rho_L} \simeq \frac{(\gamma+1)}{(\gamma-1)}, \quad \text{and } (M_L^*)^2 \simeq \frac{(\gamma-1)}{2\gamma} \tag{5}$$

where $M_L = (u_L - ws_L)/a_L >> 1$ and $M_L^* = (u_L^* - ws_L)/a_L^*$ are the Mach numbers of the gas entering and leaving the shock. Together with the expression for sound speed $a^2 = \gamma P/\rho$, these relations can be combined to eliminate ws_L and give u_L^* as a function of P^*:

$$u_L^* = u_L - \left[\frac{2P^*}{\rho_L(\gamma+1)}\right]^{1/2} \tag{6}$$

A corresponding expression can be obtained for a right-moving shock.

If $P^* > 10\,P_L$ and $P^* > 10\,P_R$, then both waves are taken to be strong shock waves and the intermediate pressure and velocity can be determined directly as

$$P^* = \frac{\gamma+1}{2}\rho_L\left[\frac{\sqrt{\rho_R}}{\sqrt{\rho_R}+\sqrt{\rho_L}}(u_L - u_R)\right]^2 \tag{7}$$

and

$$u^* = \frac{\sqrt{\rho_L}\,u_L + \sqrt{\rho_R}\,u_R}{\sqrt{\rho_R}+\sqrt{\rho_L}} \tag{8}$$

If P^* is greater than P_L or P_R (but not both), the stage 1 estimate for P^* can be improved with two Newton-Raphson steps of the form

$$P_{n+1}^* = P_n^* - F_n\left(\frac{dF_n}{dP^*}\right)^{-1}, \quad \text{where } F_n = u_L^*(P_n^*) - u_R^*(P_n^*) \tag{9}$$

and

$$u_L^* = \begin{cases} \bar{U}_L - \dfrac{2a_L}{\gamma-1}\left(\dfrac{P^*}{P_L}\right)^{\frac{\gamma-1}{2\gamma}}, & P^* \le 10P_L \\ u_L - \left[\dfrac{2P^*}{\rho_L(\gamma+1)}\right]^{1/2}, & P^* > 10P_L \end{cases} \tag{10}$$

$$u_R^* = \begin{cases} \bar{U}_R + \dfrac{2a_R}{\gamma-1}\left(\dfrac{P^*}{P_R}\right)^{\frac{\gamma-1}{2\gamma}}, & P^* \le 10P_R \\ u_R + \left[\dfrac{2P^*}{\rho_R(\gamma+1)}\right]^{1/2}, & P^* > 10P_R \end{cases} \tag{11}$$

During the update, we insure that $P^* \ge P_{\text{MIN}}$ where P_{MIN} is some small value. After updating P^*, the intermediate velocity

is evaluated using the relevant strong shock relation from Eq. (10) or (11).

C. Stage 3

Now that we have computed the pressure and velocity in the intermediate regions behind the waves, the other intermediate flow properties may be evaluated. The interface conditions used in the inviscid flux vector can then be selected or interpolated from the four flow states (L, L^*, R, R^*). Note that, although only the left-moving wave is discussed here, a similar procedure is used to obtain the flow state behind the right-moving wave.

If the pressure rises across the left-moving wave (i.e., $P^* > P_L$), the left wave is assumed to be a shock and density is obtained from the Rankine-Hugoniot relation as

$$\rho_L^* = \rho_L \left[\frac{(\gamma+1)P^* + (\gamma-1)P_L}{(\gamma+1)P_L + (\gamma-1)P^*} \right] \tag{12}$$

whereas the specific internal energy and the local speed of sound (for later use in the interpolation of the interface properties) are computed as

$$e_L^* = \frac{P^*}{(\gamma-1)\rho_L^*}, \quad \text{and } a_L^* = \sqrt{\gamma(\gamma-1)e_L^*} \tag{13}$$

The velocity of the wave (relative to the initial left state) is given by

$$u_L - ws_L = \left[\frac{\gamma+1}{2} \frac{P_L}{\rho_L} \left(\frac{P^*}{P_L} + \frac{\gamma-1}{\gamma+1} \right) \right]^{1/2} \tag{14}$$

If the pressure falls across the left-moving wave (i.e., $P^* \le P_L$), the isentropic-wave relations are used to obtain the intermediate properties. The local speed of sound is obtained from the Riemann invariant as

$$a_L^* = (\bar{U}_L - u_L^*)(\gamma-1)/2 \tag{15}$$

whereas the specific internal energy and density are computed as

$$e_L^* = \frac{(a_L^*)^2}{(\gamma-1)\gamma}, \quad \text{and } \rho_L^* = \frac{P^*}{(\gamma-1)e_L^*} \tag{16}$$

The velocity of the leading edge of the wave (relative to the initial left state) is given by

$$u_L - ws_L = a_L \tag{17}$$

III. Test Cases

A. High Mach Number Flow Around a Sphere

The robustness of the code is demonstrated by computing a Mach 60 flow over a 7.5-mm radius sphere with a domain consisting of a 60×60 mesh of cells. The $y = 0$ boundary is the symmetry line (and stagnation line) while a tangency condition is applied at the surface of the sphere. Freestream conditions of $\rho = 0.5097 \times 10^{-2}$ kg/m^3, $P = 427.1$ Pa, $e = 2.095 \times 10^5$ J/kg, $u = 20600$ m/s, $v = 0$, and $M_{\text{nominal}} = 60.1$ are applied to the curved inflow boundary, the shape of which is derived from the shock-position correlations in Ref. 8. Flow conditions at the outflow boundary are obtained by zero-order (constant) extrapolation. Initial conditions throughout the domain are set to $\rho = 0.5097 \times 10^{-2}$ kg/m^3, $P = 427.1$ Pa, $e = 2.095 \times 10^5$ J/kg, $u = 0$, and $v = 0$. Despite the very high temperatures in the shock layer, the gas is considered perfect with $\gamma = 1.4$, $R = 287$ J/kg/K, and $Pr = 0.72$, and Sutherland's law is used for the coefficient of viscosity. The Navier-Stokes equations are then integrated forward in time using high-order MUSCL interpolation and Euler time stepping with a Courant-Friedrichs-Lewy (CFL) number of 0.5.

Figure 1 shows the flowfield (pressure and Mach contours) at $t = 13.6$ μs after the flow has approached steady state. Discrete points from experimentally derived correlations[8] are plotted on the pressure contours. Given that $M = 60$ is beyond the range of the data used for the correlations, agreement is good. The largest deviations are near the outflow boundary. Profiles of density and pressure along the line of cells adjacent to the x axis are shown in Fig. 2. The shock appears to be captured in two or three cells with no oscillation, and the density jump is close to the ideal strong shock value of 6. The pressure ratio from freestream to the stagnation point is 4621, which is very close to the ideal value of 4636 for $M = 60$ (see, for example, Table II in Ref. 9).

A similar calculation with $M = 12$ was reported in Ref. 7 and, for that condition, an Osher-type solver (i.e., stages 1 and 3 only) failed to produce a solution. In addition, a finite difference scheme using Roe-type flux-difference splitting required a rather large value for its entropy-fix parameter to obtain a physically reasonable solution.[10] Although the mechanism causing the solvers to fail is not well understood, the strong shock (second) stage modification appears to make the present solver quite robust. Also note that, although the $M = 60$ shock is very strong, the high temperature in the region behind the shock enhances the viscous dissipation and may result in a smoother solution than seen at lower Mach numbers.

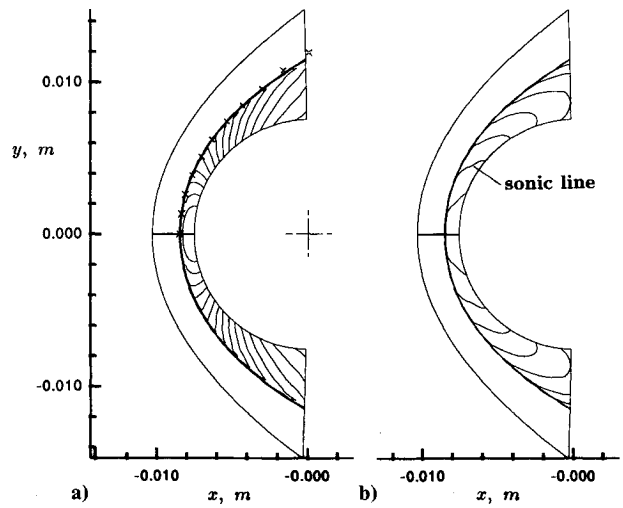

Fig. 1 $M = 60$ flow over a sphere with a tangency boundary condition: a) pressure contours, b) Mach number contours; " + " denotes the experimental correlation.

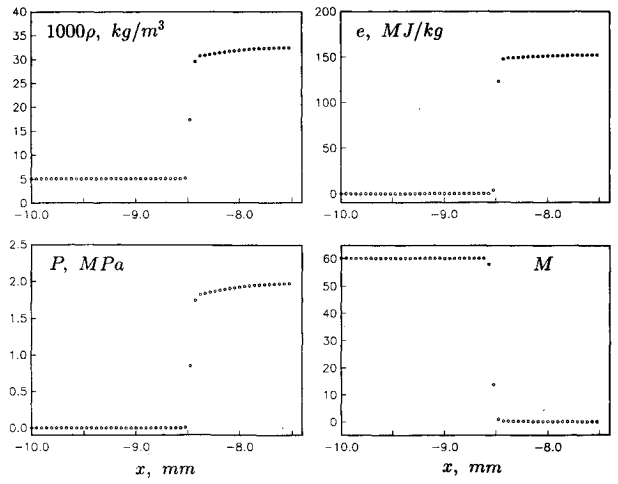

Fig. 2 Flow properties for the cells adjacent to the ($y = 0$) stagnation line.

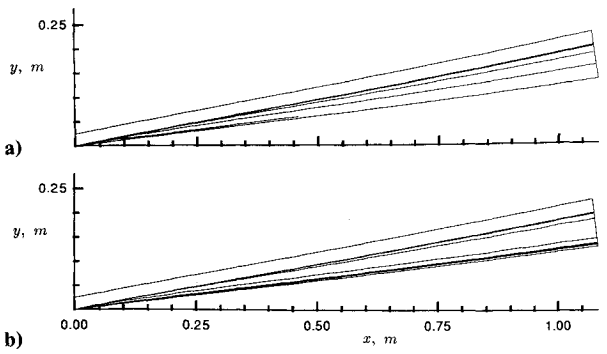

Fig. 3 Flow over a 7-deg cone with an adiabatic boundary layer: a) pressure contours, b) density contours.

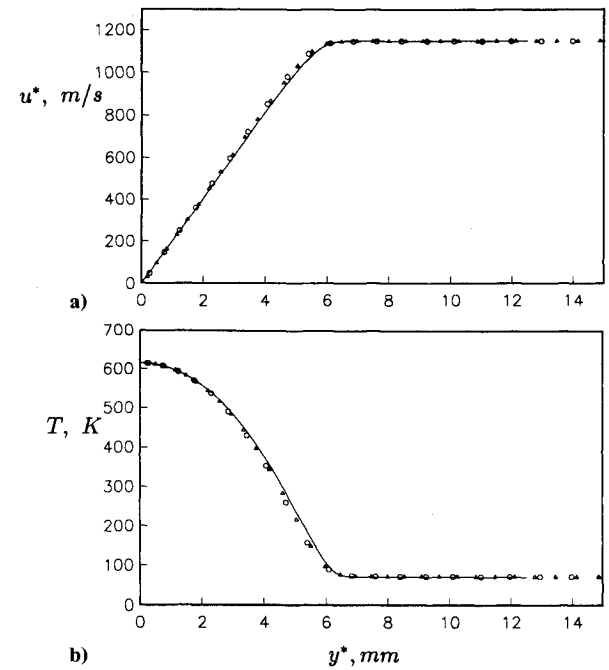

Fig. 4 Comparison of the present finite volume solution with a spectral solution at 1.0 m from the cone apex: a) tangential velocity, b) temperature. Solid line represents spectral solution, o denotes 100 × 60 mesh, △ denotes 100 × 90 mesh.

B. Flow over a Sharp Cone

To illustrate the behavior of the solver in the presence of strong viscous effects, we show the computed results for $M \simeq 8$ flow over a sharp 7-deg cone. The axis of the cone is aligned with the freestream.

Two cases are considered in which the cone flow domain is discretized as a set of 100×60 cells and 100×90 cells. Freestream conditions of $\rho = 1.0809 \times 10^{-2}$ kg/m^3, $P = 165.51$ Pa, $e = 3.8281 \times 10^4$ J/kg, $T = 53.35$ K, $u = 1164.0$ m/s, $v = 0$, and $M_{\text{nominal}} = 7.95$ are applied to the left and upper boundaries whereas the outflow boundary conditions are obtained by extrapolation, and the cone surface is modeled as a no-slip, adiabatic boundary. To match the experimental conditions in Ref. 11, the gas was considered to be a perfect gas with $\gamma = 1.4$, $R = 287$ J/kg/K, and $Pr = 0.7$, and viscosity was obtained from the Sutherland expression

$$\mu = 1.611 \times 10^{-6} \frac{T^{3/2}}{T + 110.33} \text{ Pa.s}$$

Based on freestream conditions and the length of the cone, the Reynolds number is approximately 3.3×10^6. The initial state of the flow in the domain is $\rho = 1.0809 \times 10^{-2}$ kg/m^3, $P = 165.51$ Pa, $e = 3.8281 \times 10^4$ J/kg, $u = 0$, and $v = 0$. The Navier-Stokes equations are then integrated forward in time using high-order MUSCL interpolation and Euler time stepping with a CFL number of 0.5.

Figure 3 shows the flowfield (pressure and density contours) $t = 22$ ms after the flow has approached steady state. The pressure field is almost conically symmetric, as per the inviscid solution of Taylor and Maccoll (see for example, Chap. 10 in Ref. 12), and the shock angle is still approximately the inviscid value of 10.5 deg (Ref. 9, Chart 4). The shock, however, is slightly curved near the apex of the cone. Boundary-layer profiles of velocity and temperature at $x^* = 1.0$ m are shown in Fig. 4 for both the present finite volume solutions and a boundary-layer solution using edge conditions of $\rho_e = 2.044 \times 10^{-2}$ kg/m^3, $P_e = 416.7$ Pa, $u_e^* = 1148.6$ m/s, and $T_e = 71.04$ K. There is good agreement between the present finite volume solutions and the spectrally accurate solution,[13] especially near the cone surface. Although the outer region of the boundary layer is underresolved (even for the 100×90 mesh), the finite volume solutions appear to be converging to the spectral solution.

References

[1]Gottlieb, J. J., and Groth, C. P. T., "Assessment of Riemann Solvers for Unsteady One-Dimensional Inviscid Flows of Perfect Gases," *Journal of Computational Physics,* Vol. 78, No. 2, 1988, pp. 437–458.

[2]Roe, P. L., "Approximate Riemann Solvers, Parameter Vectors, and Difference Schemes," *Journal of Computational Physics,* Vol. 43, No. 2, 1981, pp. 357–372.

[3]Osher, S., and Solomon, F., "Upwind Difference Schemes for Hyperbolic Systems of Conservation Laws," *Mathematics of Computation,* Vol. 38, No. 158, 1982, pp. 339–374.

[4]Quirk, J. J., "An Adaptive Grid Algorithm for Computational Shock Hydrodynamics," Ph.D. Thesis, College of Aeronautics, Cranfield Inst. of Technology, Bedford, England, UK, 1991.

[5]Peery, K. M., and Imlay, S. T., "Blunt-Body Flow Simulations," AIAA Paper 88-2904, 1988.

[6]Godunov, S. K., (ed.), *Numerical Solution of Multidimensional Problems in Gasdynamics,* Nauka, Moscow, 1976.

[7]Jacobs, P. A., "Single-Block Navier-Stokes Integrator," Inst. for Computer Applications in Science and Engineering, ICASE Interim Rept. 18, NASA Langley Research Center, Hampton, VA, July 1991.

[8]Billig, F. S., "Shock-Wave Shapes Around Spherical- and Cylindrical-Nosed Bodies," *Journal of Spacecraft and Rockets,* Vol. 4, No. 6, 1967, pp. 822, 823.

[9]Ames Research Staff, "Equations, Tables and Charts for Compressible Flow," NACA Rept. 1135, 1953.

[10]White, J., NASA Langley Research Center, private communication, 1991.

[11]Stetson, K. F., Thompson, E. R., Donaldson, J. C., and Siler, L. G., "Laminar Boundary Layer Stability Experiments on a Cone at Mach 8, Part 1: Sharp Cone," AIAA Paper 83-1761, 1983.

[12]Anderson, J. D., *Modern Compressible Flow: with Historical Perspective,* McGraw-Hill, New York, 1982.

[13]Pruett, C. D., and Streett, C. L., "A Spectral Collocation Method for Compressible, Nonsimilar Boundary Layers," *International Journal for Numerical Methods in Fluids,* Vol. 13, No. 6, 1991, pp. 713–737.

Grid Studies for Thin-Layer Navier-Stokes Computations of Airfoil Flowfields

D.W. Zingg*

University of Toronto Institute for Aerospace Studies, Toronto, Ontario M3H 5T6, Canada

Introduction

THE status of computational methods for viscous transonic airfoil flows is reviewed in detail in Ref. 1, which

Received Oct. 29, 1991; presented as Paper 92-0184 at the AIAA 30th Aerospace Sciences Meeting, Reno, NV, Jan. 6–9, 1992; revision received Feb. 19, 1992; accepted for publication March 30, 1992.

*Assistant Professor, 4925 Dufferin Street, Downsview, Ontario. Member AIAA.